AGU PUBLICATIONS

JGR

Journal of Geophysical Research: Oceans

RESEARCH ARTICLE

10.1002/2016JC011887

**Key Points:**
- The seasonal predictability of sea surface temperature anomalies (SSTA) in the Kuroshio-Oyashio Extension (KOE) is explored
- Perfect model predictability experiments from the viewpoint of initial error growth in a global coupled model are performed
- The mechanism responsible for error growth associated with the seasonal predictability is also explored

**Correspondence to:**
W. Duan,
duanws@lasg.iap.ac.cn

**Citation:**
Wu, Y., W. Duan, and X. Rong (2016), Seasonal predictability of sea surface temperature anomalies over the Kuroshio-Oyashio Extension: Low in summer and high in winter, *J. Geophys. Res. Oceans*, *121*, doi:10.1002/2016JC011887.

Received 27 APR 2016
Accepted 30 AUG 2016
Accepted article online 2 SEP 2016



# Seasonal predictability of sea surface temperature anomalies over the Kuroshio-Oyashio Extension: Low in summer and high in winter

**Yujie Wu[1,2], Wansuo Duan[2], and Xinyao Rong[3]**

[1]Laboratory for Climate Studies, National Climate Center, China Meteorologica Administration, Beijing, China, [2]State Key Laboratory of Numerical Modeling for Atmospheric Sciences and Geophysical Fluid Dynamics (LASG), Institute of Atmospheric Physics, Chinese Academy of Sciences, Beijing, China, [3]Chinese Academy of Meteorological Sciences, Beijing, China

**Abstract** The seasonal predictability of sea surface temperature anomalies (SSTA) in the Kuroshio-Oyashio Extension (KOE) is explored by performing perfect model predictability experiments from the viewpoint of initial error growth in a global coupled model. It is found that prediction errors of KOE-SSTA always increase in the boreal summer and decrease in the boreal winter. This leads to smaller (larger) prediction errors and higher (lower) prediction skills in boreal winter (summer). This seasonal characteristic of the KOE-SSTA error growth implies a season-dependent predictability that is lower in summer and higher in winter. The mechanism responsible for error growth associated with seasonal predictability is also explored. The error increase in summer and error decrease in winter in the KOE-SSTA are both largely attributed to the seasonal evolution of latent heat flux error and mean temperature advection by vertical current error in the KOE region, both of which are forced by the prediction error of 1 month leading zonal wind stress per unit mass for the mixed layer over the KOE region. The shallowest (deepest) mixed layer in summer (winter) amplifies (reduces) the forcing of zonal wind stress errors on the error growth of KOE-SSTA, thereby causing the seasonal evolution of prediction errors of KOE-SSTA and ultimately resulting in the season-dependent predictability of the KOE-SSTA, i.e., low in summer and high in winter.

## 1. Introduction

Accurate prediction of sea surface temperature (SST) in the North Pacific is of great importance for many societal endeavors [e.g., *Latif and Barnett*, 1994; *Englehart and Douglas*, 2003]. Recent studies of North Pacific SST predictions have generally focused on the decadal timescale because of the dominant low-frequency variability, such as the Pacific Decadal Oscillation [e.g., *Meehl and Hu*, 2006; *Meehl and Teng*, 2012; *Kim et al*., 2014; *Hu et al*., 2014]. However, the seasonal prediction skill and predictability of sea surface temperature anomalies (SSTA) in the North Pacific have received less attention. In the North Pacific, the Kuroshio-Oyashio Extension (KOE) is located in the region in which the SST variability is most significant, and the seasonal evolution of SSTA in the KOE region plays a critical role in modulating the weather and climate in North America and East Asia. For example, the summer rainfall in eastern China is most likely to be influenced by the SSTA in the KOE region in the preceding spring [*Zhu et al*., 2000; *Sun et al*., 2008]. However, several attempts have demonstrated that the seasonal prediction skill of North Pacific SSTA, especially the SSTA in the KOE region, is quite low [*Landman and Mason*, 2001; *Auad et al*., 2004; *Alexander et al*., 2008; *Wen et al*., 2012]. Therefore, exploring the seasonal predictability is very necessary for us to better understand the variability of SSTA in the KOE region and improve the prediction skill.

The persistence of sea temperature largely implies its predictability. Previous studies have examined the large-scale SSTA persistence in the North Pacific and indicated that the persistence of North Pacific SSTA is seasonally dependent, i.e., highest in winter and lowest in summer [*Namias and Born*, 1970, 1974]. *An and Wang* [2005] found that the North Pacific SSTA displays a persistence barrier during August–September. *Ding and Li* [2009] confirmed the existence of the July–September persistence barrier in the North Pacific SST. *Motokawa et al*. [2010] demonstrated that the structure of the dominant North Pacific SSTA patterns in

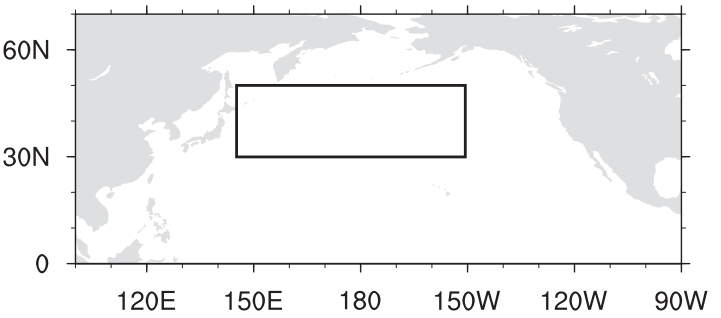


**Figure 1.** The study area. The rectangle marks the KOE-SSTA region (30°–50°N, 145°E–150°W).

the boreal summer (especially in August and September) is quite different from those in other seasons, and described an abrupt change in the evolution, indicating that the evolution of North Pacific SSTA may have its weakest memory when bestriding boreal summer. Moreover, *Zhao et al*. [2012] showed that the SSTA in the central and western Northern Pacific (i.e., the KOE region) exhibits a significant "summer persistence barrier", the phenomenon in which the persistence of SSTA shows a significant decline in the boreal summer. These results imply that the North Pacific SSTA, especially the SSTA in the KOE region, may be difficult to predict in summer. Moreover, the persistence of the North Pacific SSTA is much higher in winter. *Namias and Born* [1970, 1974] noted a tendency for midlatitude SSTA in the North Pacific to recur from one winter to the next without persisting through the intervening summer (regarded as "winter-to-winter reemergence"), which leads to the North Pacific SSTA in winter persisting for more than 1 year. The summer persistence barrier and winter-to-winter reemergence suggest season-dependent persistence of North Pacific SSTA.

The matter of how the seasonal persistence affects the forecast of North Pacific SSTA in numerical models should be addressed. It has been demonstrated that the summer persistence barrier of KOE-SSTA (the SSTA in the region 30°–50°N, 145°E–150°W; marked by the black box in Figure 1) shows itself in numerical forecasts as the "summer prediction barrier" (SPB) [*Duan and Wu*, 2015]. From the point of view of initial error growth, *Duan and Wu* [2015] pointed out that the SPB refers to the phenomenon that prediction errors of KOE-SSTA grow much more rapidly in summer and cause large prediction uncertainties, finally showing the lowest prediction skill when the forecasts bestride summer. In this paper, we further find that the KOE-SSTA shows the smallest error growth in winter (see the section 3). Therefore, we address whether the season-dependent growth of prediction errors of KOE-SSTA with the largest growth in summer and lowest in winter imply its season-dependent predictability, and whether or not the related error growth mechanism in winter is opposite to that in summer proposed by *Duan and Wu* [2015]. The answers of these questions will be helpful for us to reasonably choose the start month in the KOE-SSTA predictions and then achieve high prediction skills. Herein, we investigate these issues in a fully coupled global model by performing perfect model predictability experiments from the point of view of initial error growth. Perfect model predictability experiments involve numerical models that are assumed to be perfect, and only the effect of initial errors on the prediction uncertainties is considered [*Duan et al*., 2009]. This approach stems from studies of the first kind of predictability problems proposed by *Lorenz* [1975].

The remainder of this paper is organized as follows. In section 2, the model and approach used are described. The seasonal predictability of KOE-SSTA is reported in section 3. In section 4, we investigate the mechanisms responsible for the seasonal predictability. Finally, a summary of the key findings is presented in section 5.

## 2. Model and Approach

### 2.1. Numerical Model

The model used in this study is the fully coupled global Fast Ocean Atmosphere Model (FOAM) [*Jacob*, 1997], developed jointly at the University of Wisconsin and the Argonne National Laboratory. The atmospheric component (PCCM3-UW), with a horizontal resolution of R15 (equivalent to 7.2° longitude × 4.75° latitude) and 18 vertical levels, is a parallel version of the National Center for Atmospheric Research Community Climate Model version 2 (CCM2), but with the atmospheric physics replaced by those of CCM3. The oceanic component, with a *z*-coordinate and a resolution of 1.4° latitude × 2.8° longitude × 32 vertical levels, was developed following the Geophysical Fluid Dynamics Laboratory Modular Ocean Model. Without flux

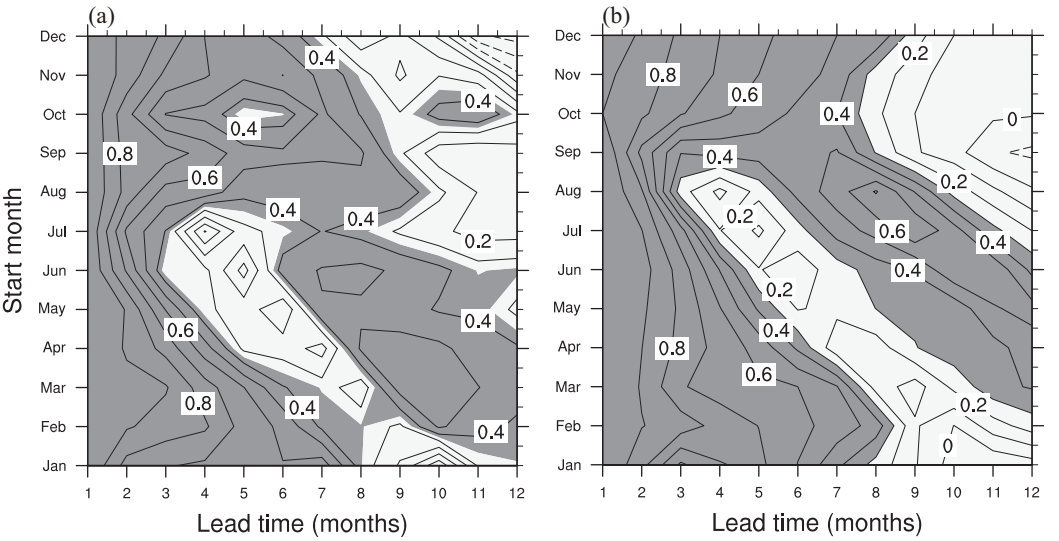


**Figure 2.** (a) The lag correlation of observed KOE-SSTA as a function of start month (ordinate) and lag month (abscissa), where the observation is from ERSST.v3b/NOAA. (b) As Figure 2a, but for FOAM-simulated KOE-SSTA. The contour interval is 0.1 and shading indicates correlation coefficients greater than the 95% confidence level.

adjustment, the fully coupled model has been integrated for over 1000 years after a spinup and we found that it does not present any apparent climate drift. FOAM has been widely used in addressing a variety of issues of tropical [e.g., *Vavrus et al*., 2006] and extratropical Pacific climate variability [e.g., *Liu and Wu*, 2004; *Yang and Liu*, 2005]. In particular, its performance in simulating the KOE-SSTA is reasonable. Figure 2 shows the lag correlation of observed and FOAM-simulated KOE-SSTA. As illustrated in Figure 2a, the persistence of the observed KOE-SSTA decreases below the 95% confidence level in summer for most of the 12 starting months and recurs in winter, implying the existence of the summer persistence barrier and winter-to-winter reemergence. FOAM-simulated KOE-SSTA shows similar features to the observations (Figure 2b). Therefore, FOAM provides us with an acceptable platform to explore the predictability of KOE-SSTA [*Duan and Wu*, 2015].

### 2.2. Experimental Strategy

*Duan and Wu* [2015] demonstrated that warm and cold KOE-SSTA occur alternately and display an oscillation cycle with a period of approximately 2–5 years; and the standard deviation of KOE-SSTA is ∼0.5 K. A warm (cold) SSTA event can thus be defined when KOE-SSTA larger (smaller) than 0.25 K (−0.25 K) persists for at least 5 months. In this study, we use the warm and cold SSTA events as the prediction targets to perform the perfect model predictability experiment and explore seasonal predictability of KOE-SSTA. Ten warm SSTA events and ten cold ones lasting 12 months in the KOE region are selected from the control run of the fully coupled simulation in FOAM. These SSTA events are regarded as the "true states" (i.e., reference states) to be predicted, and their predictions are obtained by integrating the model for 12 months with 20 perturbed initial fields starting from Nov(−1) (November(−1), i.e., November in Year(−1)), Feb(0) (February(0), i.e., February in Year(0)), May(0), and Aug(0) (August(0)). Year(0) denotes the year in which the warm and cold SSTA events attained their peak values, and Year(−1) is the year before Year(0). The perturbed initial fields are constructed with the same strategy as in *Duan and Wu* [2015]. We apply an Empirical Orthogonal Function (EOF) analysis to the North Pacific SSTA (20°–60°N, 120°E–100°W) in FOAM and obtain the first 20 EOF patterns (denoted as A1–A20) and their related PCs. The sea temperature anomalies at the 40, 60, 80 and 100m levels are then separately regressed onto the 20 PCs to obtain 20 regressed patterns for each level, denoted as B1–B20, C1–C20, D1–D20, and E1–E20. Each of the 20 EOFs along with its PC-regressed patterns in the four levels are composed of one initial error including five levels (i.e., An, Bn, Cn, Dn, and En; $n = 1, 2...20$). Then we have 20 initial sea temperature errors respectively superimposed on different starting months of the predetermined twenty SSTA events to obtain their predictions. We denote the initial errors as $T'_{0ijk}$, where $(i, j, k)$ represents grid points in the region with latitude $i$ ranging from 120°E to 100°W by 1.48°; longitude $j$ ranging from 20°N to 60°N by 2.88°; and with vertical levels $k$ of 20,40,60,80 and 100m.

We scale the initial errors $T'_{0ijk}$ to have the same magnitude using $T'_{ijk}=\sigma\cdot T'_{0ijk}/\|T'_{0ijk}\|$, in which $\|T'_{0ijk}\|=\sqrt{\sum_{i,j,k}\left(T'_{0ijk}\right)^2}$. The magnitude of the initial errors is constrained by $\|T'_{0ijk}\|=5$, which guarantees that the magnitude of initial errors is about 30–50% of the initial anomalies of the SSTA events to be predicted, and in this case the absolute value of initial error at each grid point is approximately 0.2 K on average. Therefore, a total of 400 predictions (20 events $\times$ 20 initial errors) and their related prediction errors are obtained for each of the four starting months, including 200 ones for warm events and 200 ones for cold events.

With the results of this perfect model predictability experiment, the seasonal predictability of KOE-SSTA can be investigated by analyzing the evolutionary characteristics of prediction errors. Usually, a large prediction error represents low prediction skill and fast error increase implies a rapid decline of predication skill. Therefore, large prediction error together with fast error increase indicates poor prediction skill and low predictability. The magnitude of the SSTA prediction error is calculated by $\gamma(t)=\|T^p(t)-T^r(t)\|=\sqrt{\sum_{x,y}\left(T^p_{xy}(t)-T^r_{xy}(t)\right)^2}$ [$(x,y)$ represents the longitude and latitude in the KOE region] at time $t$ ($t=1,2,\cdots 12$ *months*). $T^r(t)$ and $T^p(t)$ are the SSTA events to be predicted and their predictions, respectively. The growth tendency of prediction errors at time $t$ is computed by the slope $\kappa\ (t)=\partial\gamma(t)/\partial t$. In this study, the model outputs are the monthly means and we consider the error growth tendency from 1 month to next month. Therefore, the monthly growth tendency of prediction errors can be roughly estimated by evaluating $\kappa\ (t)\approx[\gamma\ (t+1)-\gamma(t)]/[(t+1)-t]\ =\gamma(t+1)-\gamma(t)$. A positive (negative) value of $\kappa\ (t)$ corresponds to an increase (decrease) of prediction errors, and the larger the absolute value of $\kappa\ (t)$, the faster the increase or decrease. In the following analysis, prediction error $\gamma(t)$ and error growth tendency $\kappa\ (t)$ will be used to investigate the seasonal predictability of KOE-SSTA.

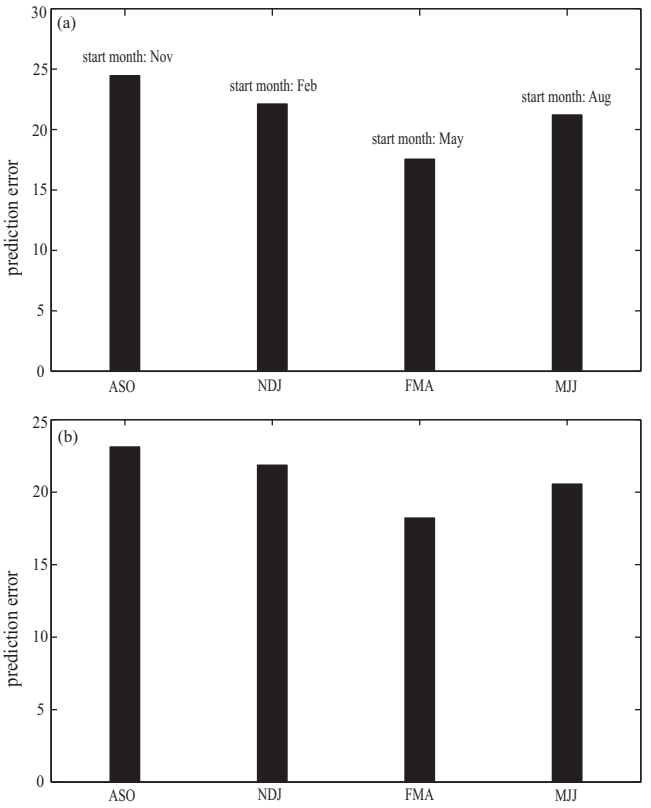


**Figure 3.** (a) Prediction errors of four target seasons, ASO, NDJ, FMA, and MJJ, predicted from start months November, February, May, and August. (b) Prediction errors of four target seasons ASO, NDJ, FMA, and MJJ, independent of start months.

## 3. Seasonal Predictability of KOE-SSTA

The perfect model predictability experiment in this study can be considered as an ensemble hindcast for four target seasons August-September-October (ASO), November-December-January (NDJ), February-March-April (FMA) and May-June-July (MJJ) with perturbed initial conditions starting from Nov(−1), Feb(0), May(0), and Aug(0), respectively. The ensemble prediction errors of four target seasons from different start months are illustrated in Figure 3a, demonstrating that the sum of prediction errors during two winter seasons (NDJ and FMA) are smaller than that in summer seasons (MJJ and ASO) with the smallest prediction errors in FMA season and the largest in ASO. Figure 3b illustrates the prediction errors in different seasons independent of start months: the results are similar to those in Figure 3a. A signal-to-noise-ratio-like measurement is used to investigate the relative prediction errors against the SSTA to be predicted, which is defined by a ratio of the prediction error variance normalized by the signal variance (the variance of

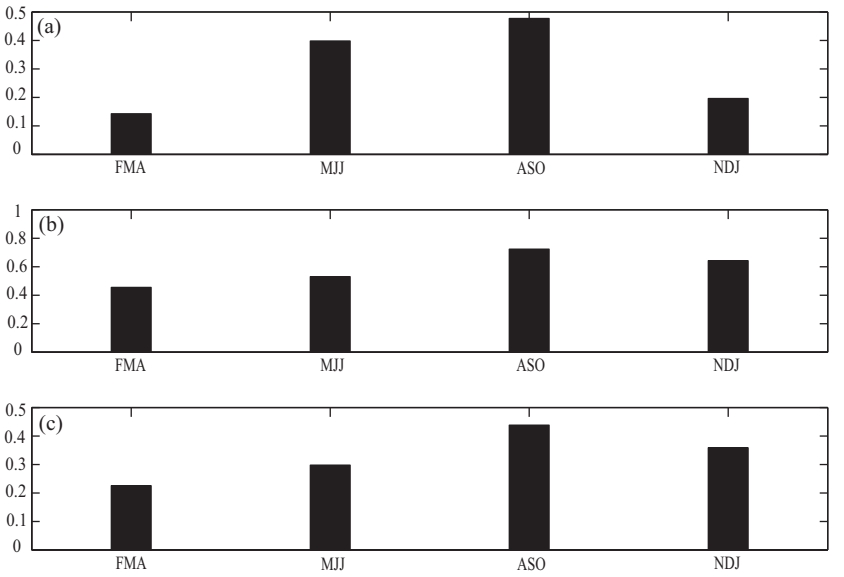


**Figure 4.** (a) The seasonal mean error-to-signal-ratio of the predicted KOE-SSTA; (b) The seasonal mean root-mean-square-error of the predicted KOE-SSTA, Unit: K. (c) As Figure 4b, but for the continuous ranked probability score, Unit: K. The results are calculated by the ensemble hindcasts from four starts months, November (−1), February (0), May (0) and August (0) in the perfect model predictability experiments.

KOE-SSTA). This ratio is denoted as error-to-signal-ratio here. In Figure 4a, we plot this ratio as a function of seasons. It is shown that the error-to-signal-ratio in winter seasons are much smaller than that in summer seasons. This suggests that the prediction errors are less likely to conceal the signal in the boreal winter than in the boreal summer, thus indicating the higher (lower) predictability of KOE-SSTA in the boreal winter (summer). The predictability are also confirmed by the measurements of root-mean-square-error (RMSE; Figure 4b) and continuous ranked probability scores (CRPS, see the Appendix A; Figure 4c). RMSE represents the sample standard deviation of the differences between predicted values and observed values and is a good measure of accuracy of prediction results. The sum of RMSE in the FMA and NDJ seasons are smaller than in the MJJ and ASO seasons, indicating a higher prediction skill in the boreal winter (Figure 4b). In Figure 4c, a smaller value of CRPS represents a better forecast of predicted distribution compared with observed distribution: therefore, the smaller values of CRPS in the winter seasons indicate a better KOE-SSTA forecast. Overall, the results illustrated in Figures 3 and 4 demonstrate that the prediction skill of KOE-SSTA is higher in the boreal winter and lower in summer.

Figure 5 shows the monthly evolution of prediction errors (colored lines) and the monthly error growth tendencies (red and blue bars) for all the predictions from four start months. The error growth tendencies are always negative from the period November to March and positive from April to October, indicating that the prediction errors always decrease during the boreal winter and increase during the boreal summer. The continuous decrease of prediction errors during the boreal winter leads to the smallest prediction error occurring at the end of winter, i.e., the FMA season (Figure 3). In the same manner, the prediction error in the ASO season (i.e., the end of summer) is larger than in the other three seasons (Figure 3) due to the continuous error increase during summer. Therefore, the decrease (increase) of prediction errors in winter (summer) causes the rise (decline) of prediction skill and explains why the prediction skill is higher (lower) in the boreal winter (summer) as shown in Figures 3 and 4.

In fact, *Duan and Wu* [2015] demonstrated that, no matter what the start month is, the largest error growth tendency (fastest error growth) often occurs in the ASO season and causes the large prediction uncertainties. This phenomenon is referred to as the "summer prediction barrier" and is considered as one of the main reasons limiting the predictability of North Pacific SSTA in the boreal summer. In this study, we further find that the error growth is smaller and the prediction skill is higher in the boreal winter than in summer, indicating a higher predictability of KOE-SSTA in the boreal winter. Therefore, combining the results of *Duan and Wu* [2015] and the present study, the large (small) prediction error together with continuous

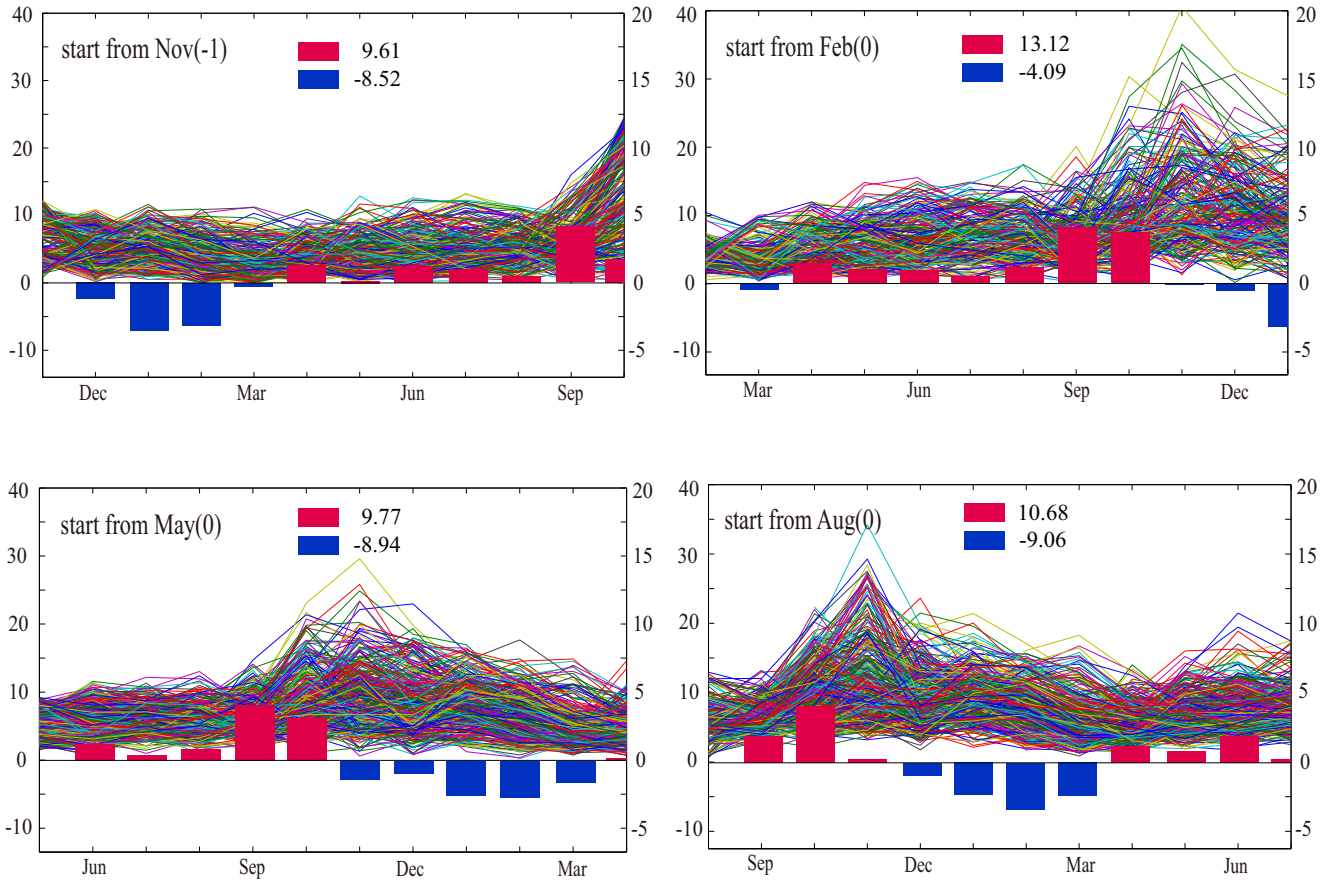


**Figure 5.** Monthly evolution of prediction errors of KOE-SSTA in terms of $\gamma(t)$ (color lines; left ordinate; each line corresponds to one initial error) and the monthly error growth tendencies $\kappa$ $(t)$ (color bars; right ordinate). The results are obtained by taking the ensemble mean of all the predictions from the start months November(−1), February(0), May(0) and August(0). The red bars represent error increase and blue bars denote an error decrease. The sums of the total error increase and total error decrease are also plotted in the figure.

decline (rise) of prediction skill during the boreal summer (winter) indicates a seasonal predictability of KOE-SSTA, i.e., higher predictability in winter and lower in summer.

In addition, it is noticed that the error increase in summer and decrease in winter are not symmetrical. In Figure 5, we find that the total error increase (sum of red bars) is larger than the total error decrease (sum of blue bars), indicating that the error increase dominates the error evolution although existing the error decrease in the predictions. The reason of this asymmetry of error growth is explained in section 4.

## 4. Possible Mechanisms for the Season-Dependent Predictability

In this section, we explain why the prediction errors of KOE-SSTA tend to increase in summer and decrease in winter. *Duan and Wu* [2015] demonstrated that the fastest error growth during the ASO season is mainly due to the largest prediction errors of latent heat flux and linear vertical oceanic temperature advection associated with the mean state in the KOE region, both of which are most likely to be driven by the prediction errors of sea surface wind stress. Naturally, we wonder whether the prediction errors of latent heat flux and linear vertical oceanic temperature advection associated with the mean state also dominate the error growth of KOE-SSTA in the other seasons (especially in winter). We also address whether the season-dependent predictability arises from the seasonal evolution of latent heat flux error and linear vertical oceanic temperature advection error associated with mean state.

Following the analysis in *Duan and Wu* [2015], we focus on the equation governing the evolution of SSTA prediction errors to trace the related error growth:

$$\frac{\partial T'}{\partial \mathrm{t}} = \frac{\partial(\bar{T}+T^{*}+T')}{\partial \mathrm{t}} - \partial\bar{T}$$

$$= \frac{Q'}{\rho c_p \bar{h}} + \left(\bar{U}_{adv} + U^*_{adv} + U^{NL}_{adv}\right) + \left(\bar{V}_{adv} + V^*_{adv} + V^{NL}_{adv}\right) + \left(\bar{W}_{adv} + W^*_{adv} + W^{NL}_{adv}\right) \quad (1)$$

in which,

$$Q' = (\bar{Q} + Q^* + Q') = LH' + SH' + LWH' + SWH' \quad (2)$$

and

$$\bar{U}_{adv} = -\bar{u}\frac{\partial T'}{\partial x} - u'\frac{\partial \bar{T}}{\partial x} \quad \bar{V}_{adv} = -\bar{v}\frac{\partial T'}{\partial y} - v'\frac{\partial \bar{T}}{\partial y} \quad \bar{W}_{adv} = -\bar{w}\frac{\partial T'}{\partial z} - w'\frac{\partial \bar{T}}{\partial z}$$

$$U^*_{adv} = -u^*\frac{\partial T'}{\partial x} - u'\frac{\partial T^*}{\partial x} \quad V^*_{adv} = -v^*\frac{\partial T'}{\partial y} - v'\frac{\partial T^*}{\partial y} \quad W^*_{adv} = -w^*\frac{\partial T'}{\partial z} - w'\frac{\partial T^*}{\partial z} \quad (3)$$

$$U^{NL}_{adv} = -u'\frac{\partial T'}{\partial x} \quad V^{NL}_{adv} = -v'\frac{\partial T'}{\partial y} \quad W^{NL}_{adv} = -w'\frac{\partial T'}{\partial z}$$

In equations (1)–(3), a bar represents the climatological mean state, an asterisk denotes the anomalies of the SSTA events to be predicted, and a prime signifies the prediction errors caused by initial errors. In equation (1), the SSTA prediction error is denoted by $T'$, and $\partial T'/\partial t$ represents the error growth tendency. $\rho$ and $c_p$ are the density of sea water and the specific heat capacity, respectively. $\bar{h}$ is the climatological monthly mean mixed-layer depth in FOAM, which, as shown in observations [*Wang et al.*, 2012], is season-dependent, being deeper in the boreal winter and shallower in the boreal summer. Equation (2) describes the effect of the net sea surface heat flux errors on the SSTA error growth, which is the sum of latent heat flux error $LH'$ (*term 1*), sensible heat flux error $SH'$ (*term 2*), shortwave radiation flux error $SWH'$ (*term 3*), and long-wave radiation flux error $LWH'$ (*term 4*). Equation (3) indicates the effect of oceanic temperature advections on the SSTA error growth, where $\bar{U}_{adv}$, $\bar{V}_{adv}$, and $\bar{W}_{adv}$ (*terms 5–7*) represent the linear zonal, meridional, and vertical oceanic temperature advection errors associated with the mean state; $U^*_{adv}$, $V^*_{adv}$, and $W^*_{adv}$ (*terms 8–10*) describe the linear oceanic temperature advection errors associated with the anomalies of SSTA events to be predicted; and $U^{NL}_{adv}$, $V^{NL}_{adv}$, and $W^{NL}_{adv}$ (*terms 11–13*) reflect the nonlinear oceanic temperature advection errors.

From equations (1)–(3), it can be approximately established that the contributions to the SSTA error growth are from the sea surface heat fluxes denoted by $Q'$ and the oceanic dynamics described by equation (3). In the following analysis, we explore how the sea surface heat fluxes and oceanic dynamics contribute to the error growth associated with the season-dependent predictability of KOE-SSTA.

### 4.1. Sea Surface Heat Fluxes and Oceanic Dynamics

According to equation (1), four kinds of sea surface heat flux errors and all types of oceanic dynamical errors, i.e., *terms 1–13* in equations (1) and (2), all contribute to the SSTA error growth. Figure 6 illustrates the contributions from *terms 1–13* to the SSTA error growth in summer (JJASO) and winter (NDJFM), which are the ensemble mean of all the predictions of the predetermined warm and cold events. In Figure 6, *term 0* is the region-mean SSTA error growth tendency (i.e., $\partial T'/\partial t$ in the left side of equation (1)). The sum of region-mean *terms 1–13* is approximately equal to *term 0*.

For warm events, a positive SSTA error growth tendency (*term 0*) in summer indicates an error increase, and a negative value indicates an error decrease. Warm events have a positive SSTA error growth tendency in summer and a negative one in winter (Figures 6a and 6b), denoting an error increase in summer and error decrease in winter. The error increase in summer is primarily dominated by the contributions of latent heat flux error $LH'$ (*term 1*) and linear vertical oceanic temperature advection error associated with mean state $\bar{W}_{adv}$ (*term 11*) (Figure 6a), which is in accordance with the results of *Duan and Wu* [2015]. In winter, the error decrease also largely arises from $LH'$ and $\bar{W}_{adv}$ (Figure 6b).

Moreover, *terms 14* and *15* denote $A = -w' \cdot \partial \bar{T}/\partial t$ and $B = -\bar{w} \cdot \partial T'/\partial t$ which make up the *term 11* (the linear vertical oceanic temperature advection error associated with mean state $\bar{W}_{adv}$). $A = -w' \cdot \partial \bar{T}/\partial t$ and $B = -\bar{w} \cdot \partial T'/\partial t$ describe the mean temperature advection by vertical current error and the temperature advection error by mean vertical current, respectively. As illustrated in Figures 6a and 6b, $A = -w' \cdot \partial \bar{T}/\partial t$ dominates the contribution of $\bar{W}_{adv}$ in both summer and winter; thus, the effects of the latent heat flux

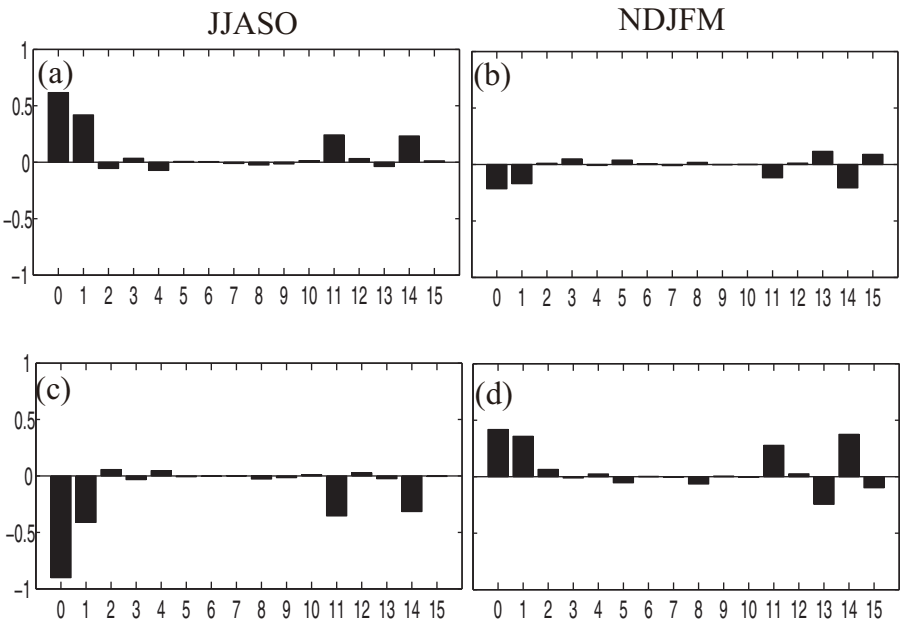


**Figure 6.** (a) The region-mean of *terms 1–15* in the KOE region in summer (JJASO), which are the ensemble means of all the predictions of predetermined KOE-SSTA warm events; (b) As Figure 6a, but for the results in winter (NDJFM). (c and d) As Figures 6a and 6b, but for the cold events. Units: K/month.

error $LH'$ and mean temperature advection by vertical current error $A=-w'\cdot\partial\bar{T}/\partial t$ to a large extent cause the error increase in summer and error decrease in winter. In addition, the nonlinear vertical oceanic temperature advection error $W_{adv}^{NL}$ (*term 13*), which is significant in winter other than in summer, has a positive value, thus favoring the SSTA error increase in winter (Figure 6b), i.e., the nonlinear vertical oceanic temperature advection error $W_{adv}^{NL}$ has the effect of suppressing the error decease in winter.

The results of cold events are similar (Figures 6c and 6d). Therefore, the latent heat flux error $LH'$ and the mean temperature advection by vertical current error $A=-w'\cdot\partial\bar{T}/\partial t$ not only cause the SSTA error increase in summer, but also lead to the error decrease in winter. Therefore, the seasonal evolutions of $LH'$ and $A=-w'\cdot\partial\bar{T}/\partial t$ are the main reasons resulting in the error increase (decrease) in the boreal summer (winter), indicating the similar but just opposite effect of the physical mechanisms for the error growth in the boreal summer and winter. There also exists difference in the mechanisms: the nonlinear vertical oceanic temperature advection error suppresses the error decrease in winter but has little effect on the error increase in summer, which therefore leads to more error increase in summer and explains the asymmetry of error growth mentioned in section 3.

### 4.2. Sea Surface Wind Stress

In fact, the sea surface wind stress errors can give rise to SSTA prediction errors in the KOE region through the latent heat flux error and the mean temperature advection by vertical current error which dominate the error increase in summer and error decrease in winter. *Duan and Wu* [2015] suggested that the anomalous northwesterly or cyclonic (southeasterly or anticyclonic) winds over the KOE region can bring dry and cold (warm and wet) air and enhance the anomalous release (absorption) of net latent heat flux, which is favorable for a negative (positive) SSTA prediction error in the KOE region. The anomalous wind stress also strengthens the upwelling (downwelling) in the KOE region, leading to the prediction errors of vertical oceanic temperature advection, ultimately causing the SSTA error growth. Moreover, previous studies have suggested that atmospheric surface wind is likely to be responsible for the evolution of North Pacific SSTA [e.g., *Newman et al.*, 2003; *Miller et al.*, 2004; *Carton et al.*, 2008]. The maximum variability of the SSTA in the KOE region in late spring and early summer is largely determined by the seasonal changes in the variance of Ekman heat flux, latent and sensible heat fluxes, and the seasonal variation of the mean mixed-layer depth (MLD). All of these

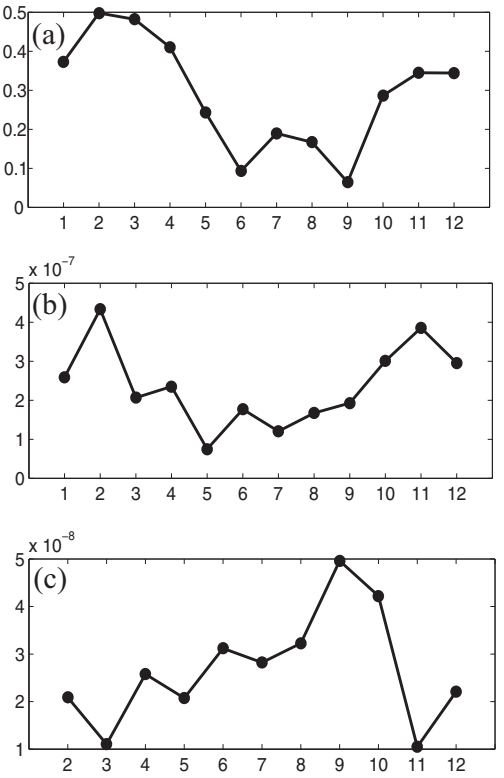


**Figure 7.** (a) The monthly signal-noise ratio of the zonal wind stress in the KOE region; (b) The monthly region-mean prediction errors of zonal wind stress averaged in the KOE region averaged by all the predictions of KOE-SSTA events. Unit: N/m$^2$; (c) The monthly prediction errors of 1 month leading zonal wind stress in KOE region divided by the climatological mean mixed-layer depth. Unit: N/m$^3$.

fluxes are closely related to the atmospheric surface wind [*Wang et al.*, 2012]. Therefore, exploring the impact of seasonal evolution of surface wind stress on the predictability of KOE-SSTA is necessary.

Firstly, we illustrate the time-dependent signal-noise ratio of the zonal wind stress in the KOE region in Figure 7a. The signal-to-noise ratio can describe the information loss of a system. The smallest signal-to-noise ratio from May to September and the largest ratio between January and April in Figure 7a indicate a minimum "predictive signal" in the boreal summer and a maximum "predictive signal" in the boreal winter, which implies a higher (lower) potential predictability in the boreal winter (summer). However, the largest prediction error of zonal wind stress averaged in the KOE region occurs in winter other than in summer (Figure 7b). This indicates that the prediction error of zonal wind stress alone clearly cannot explain the seasonal error growth of KOE-SSTA. As it is the mixed layer in the upper ocean that directly responds to the atmospheric forcing (the time scale for the SST response to atmospheric wind forcing is approximately 1 month), the MLD is also expected to play a key role in determining the effectiveness of SST response to atmospheric forcing [*Wang et al.*, 2012]. To illustrate this, Figure 7c shows the monthly prediction errors of 1 month leading zonal wind stress in the KOE region divided by the climatological mean MLD. As divided by MLD, the zonal wind stress errors display a remarkable increase in the boreal summer, attaining a peak in the ASO season, and subsequently decreasing very fast in the boreal winter, consistent with the evolution of SSTA prediction errors. Figure 7c demonstrates that the relatively small (large) prediction errors of zonal wind stress in summer (winter) may induce a large (small) SSTA prediction error over a shallower (deeper) mixed layer. This is because the influence of atmospheric forcing (zonal wind stress) on the KOE-SSTA is approximately estimated by the forcing per unit mass for the mixed layer. Therefore, the relatively larger forcing effect by prediction errors of surface wind stress induces a larger latent heat flux error and the mean temperature advection by vertical current error in the boreal summer than in the boreal winter, leading to the seasonal evolution of prediction errors, ultimately causing the season-dependent predictability of KOE-SSTA: low in summer and high in winter.

## 5. Summary and Discussion

In this paper, the predictability of KOE-SSTA in a global coupled model is explored from the viewpoint of initial error growth. By conducting perfect model predictability experiments, ten typical KOE-SSTA warm events and ten cold ones are predicted with perturbed initial conditions starting from Nov(−1), Feb(0), May(0) and Aug(0). By investigating all of the prediction errors, it is found that prediction errors of KOE-SSTA display season-dependent evolution with an error increase in the boreal summer and an error decrease in the boreal winter. Due to the continuous error increase (decrease) during the boreal summer (winter), the SSTA prediction error in summer is larger than that in winter. Moreover, it is found that the prediction skills in the boreal winter are higher than that in summer. Therefore, the larger (smaller) prediction error together with the error increase (decrease) in summer (winter) causes the decline (rise) of prediction skill, indicating a season-dependent predictability of KOE-SSTA: lower in summer and higher in winter.

The possible mechanism of the error growth associated with the season-dependent predictability is explored. It is found that latent heat flux error and linear vertical oceanic temperature advection error associated with the mean state dominate the contributions to the SSTA error growth tendency in summer as well as in winter, and they are both responsible for the error increase in summer and error decrease in winter. In addition, the nonlinear vertical temperature advection errors have the effect of suppressing the error decrease in winter, causing the error decrease in winter to be smaller than the error increase in summer. Moreover, the impact of the seasonal evolution of sea surface wind stress is also explored. The prediction error of zonal wind stress alone cannot explain the seasonal error growth of KOE-SSTA. The season-dependent predictability is strongly modulated by the seasonal variation of climatological mean MLD. The shallowest (deepest) mixed layer in summer (winter) amplifies (reduces) the forcing of zonal wind stress errors on SSTA error growth in the KOE region, leading to a relatively larger (smaller) SSTA error growth in summer (winter), ultimately causing the season-dependent predictability of KOE-SSTA.

In *Duan and Wu* [2015], the phenomenon that prediction errors exhibit significant growth in summer and cause large prediction uncertainties is referred to as the "summer prediction barrier", which can be considered as a portion of the seasonal predictability of KOE-SSTA. It is also known that there are seasonal variations in the persistence of North Pacific SSTA, referred as to the "summer persistence barrier" [*Namias and Born*, 1970, 1974; *An and Wang*, 2005; *Ding and Li*, 2009; *Zhao et al*., 2012]. *Namias and Born* [1970, 1974] discussed the physical processes responsible for the seasonal variations in the persistence of North Pacific SSTA. They speculated that the seasonal evolution of wind speed and the associated mixed-layer depth are crucial factors. The thermal anomalies in the deep winter mixed layer are difficult to alter, while the thermal anomalies in the shallow summer mixed layer tend to undergo considerable change. This physical mechanism responsible for the summer persistence barrier is similar to the one in this study. The point of difference is that this study focuses on the SSTA error growth in the KOE region. We consider that the physical mechanisms of SST anomalies and errors are similar, and the "summer prediction barrier" is a reflection of the "summer persistence barrier" in numerical forecasting.

The season-dependent predictability of KOE-SSTA, especially the "summer prediction barrier", may be one of the main factors limiting the prediction skill of the North Pacific SSTA. How to improve the prediction skills is a key issue to be addressed. The targeted observation strategy, which places additional observations in specific regions according to weather or climate event, is aimed at reducing the uncertainty of the initial conditions in specific regions and improving the skill of numerical prediction [*Mu*, 2013]. Previous studies have investigated whether the prediction can be improved by implementing additional observations over sensitive area (i.e., targeted observation area). For the well-known El Niño-Southern Oscillation (ENSO), *Morss and Battisti* [2004] suggested that observations over the eastern equatorial Pacific play an important role in forecasting ENSO with leading times of several months, using an observation system simulation experiment. *Yu et al*. [2012] utilized the conditional nonlinear optimal perturbation [*Mu et al*., 2003] method to identify sensitive areas for ENSO predictions, and found that additional observations of SST in the sensitive area could reduce the initial error of SST, and is expected to improve forecast skill. The season-dependent predictability of KOE-SSTA is very similar to the predictability of ENSO, which is apparent in numerical predictions as the spring prediction barrier. Many studies have explored the spring prediction barrier for ENSO events from the point of view of error growth [*Lau and Yang*, 1996; *Moore and Kleeman*, 1996; *Samelson and Tziperman*, 2001]: one of findings is that the spring prediction barrier of ENSO is related to the fastest growth of prediction errors during spring. Therefore, this encourages us to identify the sensitive area of KOE-SSTA predictions in future work, in an attempt to provide useful information for improving the forecast skill of KOE-SSTA. Moreover, this study emphasizes the important roles of wind stress and mixed-layer depth on the dynamics of the coupled ocean-atmosphere system, which also have been demonstrated in previous theoretical works in an idealized coupled model [*Gallego and Cessi*, 2009] and in a low-order coupled ocean-atmosphere model [*Vannitsem*, 2015]. Therefore, pursuing the current work in the more theoretical models may contribute to the deeper understanding of the ocean-atmosphere system in the North Pacific.

## Appendix A: Continuous Rank Probability Score (CRPS)

Let the parameter of interest be denoted by $\boldsymbol{x}$. For instance, $\boldsymbol{x}$ could be KOE-SSTA in the paper. The continuous ranked probability score [*Brown*,1974*; Matheson and Winkler*, 1976*; Unger*, 1985], expressing one kind of distance between the probabilistic forecast and truth, is defined as

$$\mathrm{CRPS}=\frac{1}{ncases}\sum_{i=1}^{ncases}\int_{-\infty}^{\infty}\left(F_i^f(x)-F_i^o(x)\right)^2 dx.$$

Here $\boldsymbol{F_i^f(x)}$ is the cumulative distribution function (CDF) of forecast probability for the $\boldsymbol{i^{th}}$ forecast case and $\boldsymbol{F_i^o(x)}$ is the CDF of observation.

The CRPS measures the closeness of the predicted and occurred cumulative distributions. Its minimal value of zero is only achieved for $\boldsymbol{F_i^f(x)=F_i^o(x)}$, that is, in the case of a perfect deterministic forecast.

In practice, the CRPS is often computed discretely, since observations and forecast distributions are reported in discrete intervals. The reference *Hersbach* [2000] gives useful guidance on the computation of the score using a discrete representation of the forecast CDF.

**Acknowledgments**
The authors are grateful for the insightful comments and constructive suggestions provided by the three anonymous reviewers. This job was jointly sponsored by the National Natural Science Foundation of China (grant 41376018), the National Basic Research Program of China (grant 2012CB955202). The ERSST.v3b data used in this study are available at http://www.ncdc.noaa.gov/data-access/.

## References

Alexander, M. A., L. Matrosova, C. Penland, J. D. Scott, and P. Chang (2008), Forecasting Pacific SSTs: Linear inverse model predictions of the PDO, *J. Clim.*, *21*, 385–402.
An, S. I., and B. Wang (2005), The forced and intrinsic low-frequency modes in the North Pacific, *J. Clim.*, *18*, 876–885, doi:10.1175/JCLI-3298.1.
Auad, G., A. J. Miller, and J. O. Roads (2004), Pacific Ocean forecasts, *J. Mar. Syst.*, *45*, 75–90.
Brown, T. A. (1974), *Admissible Scoring Systems for Continuous Distributions*, 22 pp., Rand Corp., Santa Monica, Calif.
Carton, J. A., S. A. Grodsky, and H. Liu (2008), Variability of the ocean mixed layer, 1960–2004, *J. Clim.*, *21*, 1029–1047.
Ding, R. Q., and J. P. Li (2009), Decadal and seasonal dependence of North Pacific SST persistence, *J. Geophys. Res.*, *114*, D01105, doi:10.1029/2008JD010723.
Duan, W. S., and Y. J. Wu (2015), Season-dependent predictability and error growth dynamics of Pacific Decadal Oscillation-related sea surface temperature anomalies, *Clim. Dyn.*, *44*, 1053–1072, doi:10.1007/s00382-014-2364-5.
Duan, W. S., X. Liu, K. Y. Zhu, and M. Mu (2009), Exploring initial errors that cause a significant spring predictability barrier for El Niño events, *J. Geophys. Res.*, *114*, C04022, doi:10.1029/2008JC004925.
Englehart, P. J., and A. V. Douglas (2003), Assessing warm season drought episodes in the central United States. *J. Climate*, *16*, 1831–1842.
Gallego, B., and P. Cessi (2000), Exchanges of heat and momentum between the atmosphere and the ocean: A minimal model of decadal oscillations, *Climate Dynamics*, *16*, 479–489.
Hersbach, H. (2000), Decomposition of the continuous ranked probability score for ensemble prediction systems, *Weather Forecasting*, *15*(5), 559–570.
Hu, Z. Z., A. Kumar, B. Huang, J. Zhu, and Y. Guan (2014), Prediction skill of North Pacific variability in NCEP climate forecast system version 2: Impact of ENSO and beyond, J. Clim., *27*, 4263–4272.
Jacob, R. L. (1997), Low frequency variability in a simulated atmosphere-ocean system, PhD thesis, p. 155, Univ. of Wis.-Madison.
Kim, H. M, Y.-G. Ham, and A. A. Scaife (2014), Improvement of initialized decadal predictions over the North Pacific Ocean by systematic anomaly pattern correction, *J. Clim.*, *27*, 5148–5162.
Landman, W. A., and S. J. Mason (2001), Forecasts of near-global sea surface temperatures using canonical correlation analysis, *J. Clim.*, *14*(18), 3819–3833.
Latif, M., and T. P. Barnett (1994), Causes of decadal climate variability over the North Pacific and North America. *Science*, *266*, 634.
Lau, K. M., and S. Yang (1996), The Asian monsoon and predictability of the tropical ocean-atmosphere system, *Q. J. R. Meteorol. Soc.*, *122*, 945–957.
Liu, Z., and L. Wu (2004), Atmospheric response to the North Pacific SST: The role of ocean-atmosphere coupling, *J. Clim.*, *17*, 1859–1882.
Lorenz, E. N. (1975), Climate predictability: The physical basis of climate modelling, *Global Atmos. Res. Programme Publ. Ser. 16*, pp. 132–136, World Meteorol.Org., Geneva, Switzerland.
Matheson, J. E., and R. L.Winkler (1976), Scoring rules for continuous probability distributions, *Manage. Sci.*, *22*, 1087–1095.
Meehl, G. A., and A. Hu (2006), Megadroughts in the Indian monsoon region and southwest North America and a mechanism for associated multidecadal Pacific sea surface temperature anomalies, *J. Clim.*, *19*, 1605–1623.
Meehl, G. A., and H. Teng (2012), Case studies for initialized decadal hindcasts and predictions for the Pacific region, *Geophys. Res. Lett.*, *39*, L22705, doi:10.1029/2012GL053423.
Miller, A. J., F. Chai, S. Chiba, J. R. Moisan, and D. J. Neilson (2004), Decadal-scale climate and ecosystem interactions in the North Pacific Ocean, *J. Oceanogr.*, *60*, 163–188.
Moore, A. M., and R. Kleeman (1996), The dynamics of error growth and predictability in a coupled model of ENSO, *Q. J. R. Meteorol. Soc.*, *122*, 1405–1446.
Morss, R. E., D. S. Battisti (2004), Evaluating observing requirements for ENSO prediction: Experiments with an intermediate coupled model, *J. Clim.*, *17*, 3057–3073.
Motokawa, N., N. Matsuo, and N. Iwasaka (2010), Dominant sea-surface temperature anomaly patterns in summer over the North Pacific Ocean, *J. Oceanogr.*, *66*, 581–590.
Mu, M. (2013), Methods, current status, and prospect of targeted observation, *Sci. China Earth Sci.*, *56*, 1997–2005, doi:10.1007/s11430-013-4727-x.
Mu, M., W. S. Duan, and B. Wang (2003), Conditional nonlinear optimal perturbation and its applications, *Nonlinear Processes Geophys.*,*10*, 493–501.
Namias, J., and R. M. Born (1970), Temporal coherence in North Pacific sea surface temperature patterns, *J. Geophys. Res.*, *75*, 5952–5955.
Namias, J., and R. M. Born (1974), Further studies of temporal coherence in North Pacific sea surface temperature patterns, *J. Geophys. Res.*, *79*, 797–798.
Newman, M., G. P. Compo, and M. A. Alexander (2003), ENSO-forced variability of the Pacific decadal oscillation, *J. Clim.*, *16*, 3853–3857.
Samelson, R. G., and E. Tziperman (2001), Instability of the chaotic ENSO: The growth-phase predictability barrier, *J. Atmos. Sci.*, *58*, 3613–3625.

Sun, J. Q., W. Yuan, and Y. Gao (2008), Arabian Peninsula-North Pacific Oscillation and its association with the Asian summer monsoon, *Sci. China Ser. D Earth Sci.*, *51*, 1001–1012.

Unger, D. A. (1985), A method to estimate the continuous ranked probability score. in *Ninth Conference on Probability and Statistics in Atmospheric Sciences*, pp. 206–213, Am. Meteorol. Soc., Virginia Beach, Va.

Vannitsem, S. (2015), A dynamical system's perspective of the role of the ocean mixed layer on the development of the North Atlantic Oscillation, *Geophys. Res. Lett.*, *42*, 8615–8623.

Vavrus, S., M. Notaro, and Z. Liu (2006), A mechanism for abrupt climate change associated with tropical Pacific SSTs, *J. Clim.*, *19*, 242–256.

Wang, H., A. Kumar, W. Wang, and Y. Xue (2012), Seasonality of the Pacific decadal oscillation, *J. Clim.*, *25*(1), 25.

Wang, Q., M. Mu, and H. A. Dijkstra (2012), Application of the conditional nonlinear optimal perturbation method to the predictability study of the Kuroshio large meander, *Adv. Atmos. Sci.*, *29*(1), 118–134.

Wen, C. H., Y. Xue, and A. Kumar (2012), Seasonal prediction of North Pacific SSTs and PDO in the NCEP CFS hindcasts, *J. Clim.*, *25*, 5689–5710.

Yang, H., and Z. Liu (2005), Tropical-extratropical climate interaction as revealed in idealized coupled climate model experiments, *Clim. Dyn.*, *24*(7-8), 863–879.

Yatagai, A., and T. Yasunari (1994), Trends and decadal-scale fluctuations of surface air temperature and precipitation over China and Mongolia during the recent 40 year period (1951-1990), *J. Meteorol. Soc. Jpn.*, *72*, 937–957.

Yu, Y. S., M. Mu, W. S. Duan, and T. Gong (2012), Contribution of the location and spatial pattern of initial error to uncertainties in El Niño predictions, *J. Geophys. Res.*, *117*, C06018, doi:10.1029/2011JC007758.

Zhao, X., J. P. Li, and W. J. Zhang (2012), Summer persistence barrier of sea surface temperature anomalies in the central western North Pacific, *Adv. Atmos. Sci.*, *29*(6), 1159.